physica status solidi b
www.pss-b.com

High-Pressure Stability and Superconductivity of Clathrate Thorium Hydrides

*Shichang Yao, Chongze Wang, Hyunsoo Jeon, Liangliang Liu, Jin Mo Bok, Yunkyu Bang, Yu Jia, and Jun-Hyung Cho**

Recently, thorium hydride ThH_9 possessing a H-rich clathrate structure has been experimentally synthesized to exhibit a superconducting transition temperature T_c of 146 K at 170–175 GPa, while the more H-rich clathrate thorium hydride ThH_{18} is theoretically predicted to reach a T_c of 296 K at 400 GPa. Using first-principles calculations, it is found that ThH_9 has a more ionic character between Th atoms and H cages than ThH_{18} and that the latter has a more substantial hybridization of the Th 6*p* semicore and H 1*s* states than the former. These different bonding characteristics of ThH_9 and ThH_{18} reflect the very large difference in their stabilization pressures. Furthermore, it is revealed that the H-derived density of states at the Fermi level E_F is about two times larger in ThH_{18} than in ThH_9, which in turn leads to the significant large differences in the electron–phonon coupling (EPC) constant and T_c between the two thorium hydrides. The findings not only present the different bonding and EPC characteristics of ThH_9 and ThH_{18} but also have important implications for the design of H-rich, high-T_c clathrate metal hydrides.

1. Introduction

The realization of room-temperature superconductivity (SC) is one of the grand challenges in condensed matter physics.[1–3] An early theoretical proposal[4] of high-temperature SC began with the atomic metallic hydrogen that can be transformed from molecular insulating hydrogen under high pressures.[5,6] However, the experimental realization of atomic metallic hydrogen has been very difficult,[1–3] because it requires careful characterization of the material at very high pressures (≈500 GPa and above), which is currently challenging for diamond anvil cells.[7,8] To achieve such a hydrogen-driven metallic state at relatively lower pressures, an alternative approach has been devised using hydride materials[9] in which hydrogen atoms can be "chemically precompressed" through interactions with other constituent atoms.[10,11] This approach has recently been demonstrated to be viable for the realization of near room-temperature SC at much lower pressures below 200 GPa.[12–17]

Motivated by the previous theoretical predictions of high superconducting transition temperatures T_c in compressed hydrides,[18–29] intensive experimental efforts have been made for the synthesis of various hydrides such as sulfur hydride H_3S,[12] rare-earth/actinide hydrides MH_n (M = La,[13,14] Y,[15–17] Ce,[30–32] and Th[33]), and alkaline earth hydride CaH_6.[34,35] Specifically, the latter two families of metal hydrides have H-rich clathrate structures, where each metal atom is surrounded by the H cage composed of a large number of H atoms, that is, 24, 29, and 32 H atoms for $n = 6$, 9, and 10, respectively. These H-rich clathrate metal hydrides exhibit a wide range of T_c depending on metal elements. For example, LaH_{10} was experimentally observed to exhibit a T_c of 250–260 K at pressures of 170–190 GPa[13,14] and subsequently YH_6 was measured

S. Yao, L. Liu, Y. Jia
Joint Center for Theoretical Physics
School of Physics and Electronics
Henan University
Kaifeng 475004, P. R. China

S. Yao, C. Wang, H. Jeon, J.-H. Cho
Department of Physics and Research Institute for Natural Science
Hanyang University
222 Wangsimni-ro, Seongdong-Ku, Seoul 04763, Republic of Korea
E-mail: chojh@hanyang.ac.kr

The ORCID identification number(s) for the author(s) of this article can be found under https://doi.org/10.1002/pssb.202300451.

DOI: 10.1002/pssb.202300451

L. Liu, Y. Jia
Key Laboratory for Special Functional Materials of the Ministry of Education
Henan University
Kaifeng 475004, P. R. China

J. M. Bok, Y. Bang
Department of Physics
Pohang University of Science and Technology
Pohang 37673, Republic of Korea

Y. Bang
Asia Pacific Center for Theoretical Physics (APCTP)
Pohang-si, Gyeongsangbuk-do 37673, Republic of Korea

to exhibit $T_c = 220$ K at 166 GPa,[15,16] YH_9, $T_c = 243$ K at 201 GPa,[16,17] ThH_{10}, $T_c = 159$ K at 174 GPa,[33] and CaH_6, $T_c = 215$ K at 170 GPa.[34,35]

Recently, Zhong et al.[36] used a crystal structure search method to find a new class of extremely H-rich clathrate rare-earth/actinide hydrides MH_{18} (M = Y, La, Ce, Ac, and Th). Among them, the heaviest element Th hydride ThH_{18} was predicted to exhibit a T_c of 296 K at 400 GPa. Interestingly, these values of T_c and stabilization pressure in ThH_{18} are much higher than the experimental data ($T_c = 146$ K at 170 GPa) in ThH_9 having half of hydrogen content.[33] Zhong et al.[36] explained the existence of the higher T_c in ThH_{18} in terms of the increased electronic density of states (DOS) at the Fermi level E_F, the large phonon energy scale of the vibration modes, and the resulting enhanced electron–phonon coupling (EPC). Although these factors are essential for increasing T_c in conventional phonon-mediated Bardeen–Cooper–Schrieffer[37] superconductors, more quantitative analysis is desired to explain the significant T_c difference between ThH_9 and ThH_{18}, as discussed below. Furthermore, understanding the significantly different bonding characteristics of ThH_9 and ThH_{18}, which may reflect the very large difference in their stabilization pressures, is valuable in searching for H-rich, high-T_c clathrate metal hydrides.

In this article, based on first-principles calculations, we investigate the origin of the very large differences in the stabilization pressure and T_c between ThH_9 and ThH_{18}. For this, we compare the structural, electronic, phononic, and superconducting properties of ThH_9 and ThH_{18} compressed at 130 and 400 GPa, respectively. Compared to ThH_{18}, ThH_9 has a greater ionic character with more charge transfer from Th to H atoms, while ThH_{18} has substantially delocalized Th 6*p* semicore states at a high pressure of 400 GPa, leading to their strong hybridization with the H 1*s* state. These different bonding characteristics of ThH_9 and ThH_{18} reflect a significant difference in their stabilization pressures. Furthermore, we reveal that ThH_{18} has about two times larger H-derived DOS at E_F and ≈29% higher average-squared H-derived phonon frequency than ThH_9, but the two hydrides have similar Fermi-surface average-squared electron–phonon matrix element. As a result, the EPC constant λ and T_c of ThH_{18} are estimated as 2.08 and 269 K, respectively, which are greater than those (1.55 and 151 K) of ThH_9.

2. Computational Methods

Our DFT calculations were performed using the Vienna ab initio simulation package with the projector-augmented wave (PAW) method.[38–40] For the exchange-correlation energy functional, we employed the generalized-gradient approximation of Perdew–Burke–Ernzerhof.[41] We treated Th $6s^26p^65f^16d^17s^2$ and H $1s^1$ as valence electrons, including $6s^26p^6$ semicore electrons for Th. A planewave basis was used with a kinetic energy cutoff of 500 eV. The *k*-space integration of ThH_9 (ThH_{18}) was done with the $18 \times 18 \times 12$ ($8 \times 8 \times 8$) *k* points for the structure optimization and the $24 \times 24 \times 18$ ($18 \times 18 \times 18$) *k* points for DOS calculation. All atoms were allowed to relax along the calculated forces until all the residual force components were less than 0.001 eV $Å^{-1}$. We calculated the phonon spectrum of ThH_9 (ThH_{18}) using the QUANTUM ESPRESSO package,[42] where ultrasoft pseudopotentials,[43] a kinetic energy cutoff of 1088 eV, $18 \times 18 \times 12$ ($8 \times 8 \times 8$) *k* points, and $6 \times 6 \times 4$ ($2 \times 2 \times 2$) *q* points were employed. Here, the structural optimizations of ThH_9 or ThH_{18} using PAW and ultrasoft pseudopotentials give rise to similar lattice parameters and band structures (see Figure S1, Supporting Information).[44] For the EPC calculation, we used the software EPW[45,46] with the $12 \times 12 \times 8$ ($6 \times 6 \times 6$) *q* and $24 \times 24 \times 16$ ($24 \times 24 \times 24$) *k* points for ThH_9 (ThH_{18}).[47]

3. Results and Discussion

We begin by optimizing the structures of ThH_9[33] and ThH_{18}[36] using first-principles DFT calculations. **Figure 1**a,b shows the optimized structures of ThH_9 and ThH_{18} at 130 GPa and 400 GPa, respectively. Hereafter, we focus on the comparison of the structural, electronic, phononic, and superconducting

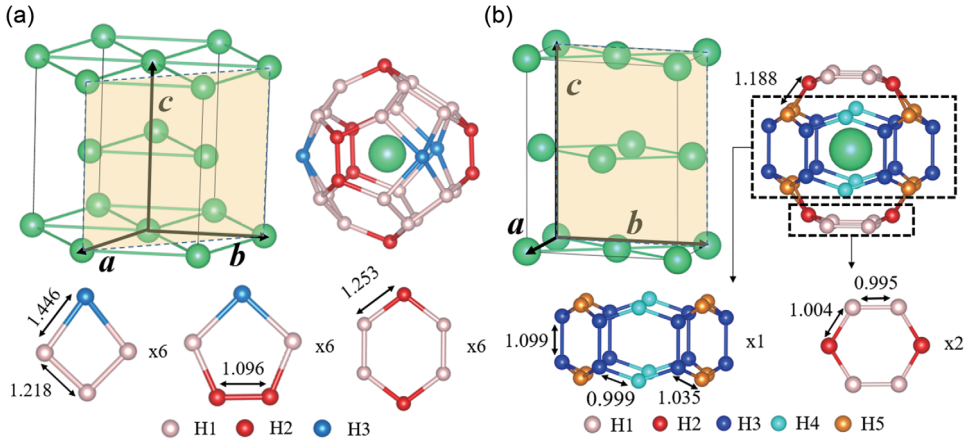

Figure 1. Optimized structures of a) ThH_9 at 130 GPa and b) ThH_{18} at 400 GPa. The Th sublattice in ThH_9 (ThH_{18}) forms the hcp (centered rectangular) lattice with the H_{29} (H_{36}) cage surrounding each Th atom. The H_{29} cage is composed of six tetragon, six pentagon, and six hexagon rings, while the H_{36} cage is composed of the strip of six hexagon rings and two wrinkled hexagon rings. There are three (five) different types of H atoms in ThH_9 (ThH_{18}), which are identified by Wyckoff positions.[33,36] The (110) and (100) planes are drawn in the hcp and centered rectangular lattices, respectively.

properties of these two compressed structures. For ThH_9, the Th sublattice forms the hexagonal closed packed (hcp) lattice with the lattice constants $a = b = 3.726$ Å and $c = 5.565$ Å (see Figure 1a), where the H_{29} clathrate cage surrounding a Th atom consists of six tetragon, six pentagon, and six hexagon rings. Meanwhile, the Th sublattice in ThH_{18} forms the centered rectangular lattice with $a = 3.357$ Å, $b = 5.826$ Å, and $c = 7.180$ Å (see Figure 1b), where the H_{36} clathrate cage surrounding a Th atom consists of the strip of six hexagon rings and two wrinkled hexagon rings above and below the strip. It is worth noting that ThH_9 has four different H—H bond lengths of 1.096, 1.218, 1.253, and 1.446 Å (see Figure 1a). In contrast, the H—H bond lengths in ThH_{18} are relatively shortened with a range of 0.995–1.188 Å (see Figure 1b), which in turn increases the maximum H-derived phonon frequency compared to that of ThH_9, as will be shown later.

Figure 2a,b shows the calculated band structures of ThH_9 and ThH_{18}, respectively. It is seen that the band projections onto Th and H atoms in ThH_9 (ThH_{18}) represent their strong hybridization over the entire energy range between −21.4 (−28.2) eV and E_F. To explore the Th—H hybridization in detail, we present the partial DOS (PDOS) of ThH_9 and ThH_{18} in Figure 2c,d, respectively. In contrast to ThH_9 having the rather localized Th 6*p* semicore states around −20 eV below E_F, ThH_{18} has the substantially delocalized Th 6*p* semicore states that strongly hybridize with the H 1*s* state in a wide energy range from ≈−28 to ≈−17 eV. Such a large delocalization of Th 6*p* semicore electrons in ThH_{18} is likely due to the increased interactions between Th atom and its surrounding H atoms at a high pressure of 400 GPa.[48,49] Note that the distances between Th and H atoms in ThH_{18} are shortened with a range of 1.88–2.04 Å, compared to those (2.08–2.23 Å) in ThH_9. Therefore, the strong hybridization of the Th semicore and H 1*s* states in ThH_{18} could be an essential ingredient for the stabilization of the large H_{36} clathrate cage.[50] The right panels in Figure 2c,d display a closeup of the Th- and H-derived DOS around E_F. For ThH_{18}, we find a van Hove

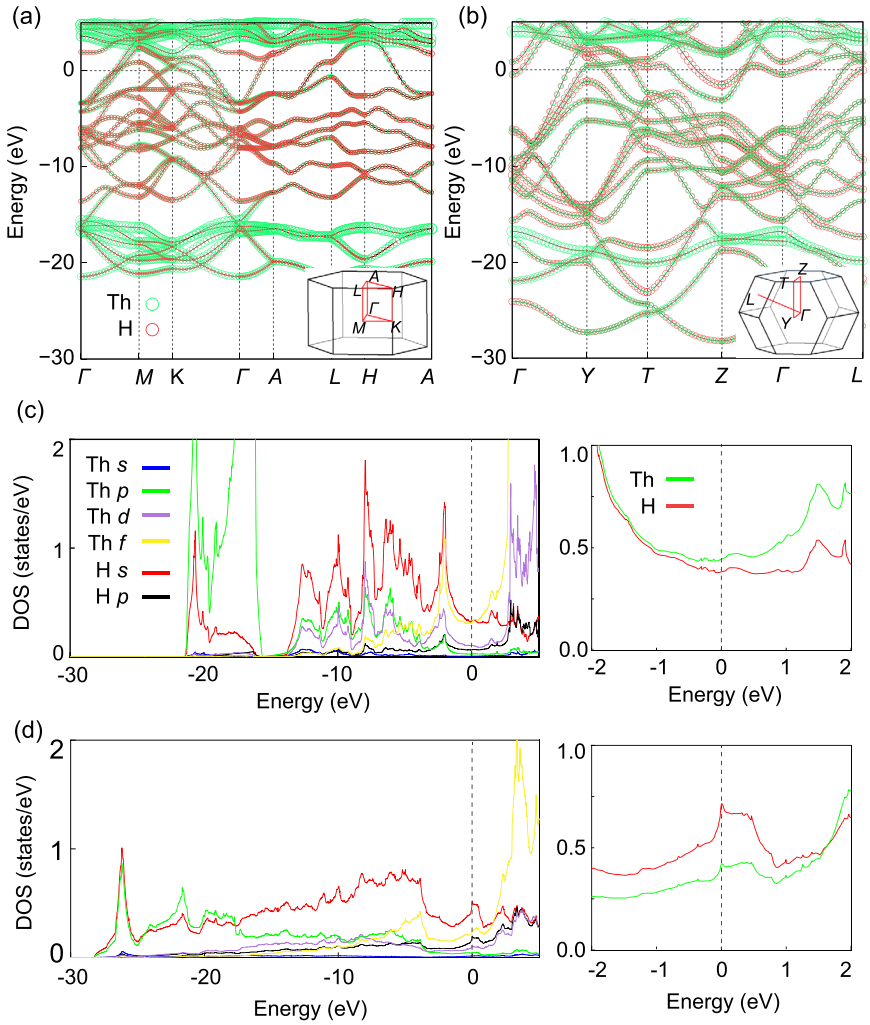

Figure 2. Calculated band structures of a) ThH_9 at 130 GPa and b) ThH_{18} at 400 GPa. The projected bands onto Th and H atoms are represented by circles whose radii are proportional to the weights of the corresponding atoms. The energy zero represents E_F. The Brillouin zones corresponding to the primitive cells of ThH_9 and ThH_{18} are included in (a,b), respectively. The PDOS results (in the unit of states/eV per unit cell) for the Th and H orbitals of ThH_9 and ThH_{18} are displayed in (c,d), respectively. The right panels in (c,d) enlarge the PDOS sums for Th and H atoms around E_F.

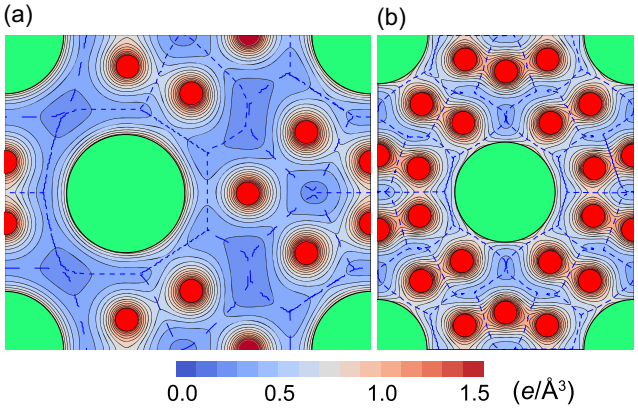

Figure 3. Calculated total charge densities of a) ThH_9 and b) ThH_{18}, together with the Bader basins of Th and H atoms. The green and red circles represent Th and H atoms, respectively. The charge densities in (a,b) are plotted on the (110) and (100) planes (see Figure 1a,b) with the contour spacing of 0.1 e Å^{-3}, respectively.

singularity at E_F, giving rise to an H-derived DOS of 0.715 states/eV at E_F. This magnitude of H-derived DOS is ≈1.87 times larger than 0.382 states/eV for ThH_9.[51] Such a large difference of the H-derived DOS at E_F between ThH_9 and ThH_{18} mainly contributes to a significant difference in their T_c values, as discussed below.

It is well established that H-rich clathrate metal hydrides have an ionic character between metal and H atoms due to their charge transfer.[52,53] To estimate the charge transfer from Th to H atoms, we analyze their Bader charges[54] in ThH_9 and ThH_{18}. **Figure 3**a,b shows the calculated total charge densities of ThH_9 and ThH_{18} with the Th/H Bader basins,[54] respectively. Here, the Bader basins are obtained from a computation of the gradient of the total charge density.[55,56] The estimated cationic/anionic charges within the Th/H Bader basins are summarized in **Table 1**. We find that the Th cationic charge in ThH_9 is 1.68e, larger than that (1.44e) in ThH_{18}. Accordingly, the sum of the anionic charges of different H atoms in ThH_9 is larger in magnitude than that in ThH_{18}. Therefore, ThH_9 has a more ionic character between Th and H atoms, compared to ThH_{18}. Meanwhile, ThH_{18} having a less ionic character between Th and H atoms would stabilize the extremely H-rich H_{36} cage via the strong hybridization between the Th 6p semicore and H 1s states at a high pressure of 400 GPa.

Next, we examine the phonon spectra of ThH_9 and ThH_{18} using density functional perturbation theory calculations.[40] **Figure 4**a,b shows the calculated phonon dispersions of ThH_9 and ThH_{18}, respectively.[57] The projected DOS onto Th and H atoms shows that, for both ThH_9 and ThH_{18}, the acoustic

Table 1. Estimated cationic/anionic charges (in unit of e) within the Bader basins of th/h atoms in ThH_9 and ThH_{18} (see Figure 3a,b). The numbers in parentheses represent the number of different H atoms in each formula unit.

	Th	H1	H2	H3	H4	H5
ThH_9	1.68	−0.26(1)	−0.09(2)	−0.21(6)	–	–
ThH_{18}	1.44	−0.10(4)	−0.02(4)	−0.02(4)	−0.15(4)	−0.15(2)

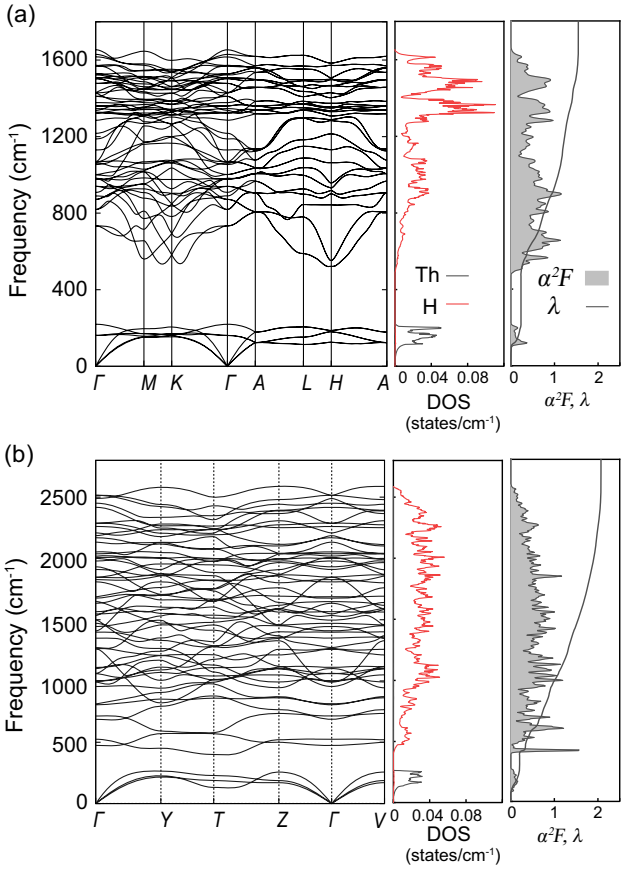

Figure 4. Calculated phonon spectra, phonon DOS projected onto Th and H atoms, $\alpha^2F(\omega)$, and $\lambda(\omega)$ of a) ThH_9 and b) ThH_{18}.

phonon modes of Th atoms are well separated from the optical phonon modes of H atoms. We find that the H-derived phonon modes in ThH_9 are distributed between 496 and 1655 cm^{-1} (see Figure 4a), while those in ThH_{18} reside in a wide frequency range from 397 to 2587 cm^{-1} (see Figure 4b). Therefore, the H-derived phonon modes in ThH_{18} exhibit not only hardening of the high-frequency regime but also softening of the low-frequency regime, compared to those in ThH_9. The former (latter) hardening (softening) is likely caused by the shorter H—H (Th—H) bond lengths in ThH_{18} (see Figure 1b). As a result, we find that the logarithmic average ω_{log} of H-derived phonon frequencies in ThH_{18} is 1034 cm^{-1}, higher than that (885 cm^{-1}) in ThH_9 (see **Table 2**).

Using the isotropic Migdal–Eliashberg formalism,[58–60] we calculate the Eliashberg spectral function $\alpha^2F(\omega)$ and integrated EPC constant $\lambda(\omega)$ as a function of phonon frequency. Figure 4a, b shows the comparison of $\alpha^2F(\omega)$ and $\lambda(\omega)$ between ThH_9 and ThH_{18}. We find that for the two hydrides, all the phonon modes including the Th-derived acoustic and H-derived optical modes, contribute to increasing $\lambda(\omega)$. For ThH_9 (ThH_{18}), the Th-derived acoustic modes are estimated to contribute to ≈15 (10)% of the total EPC constant $\lambda = \lambda(\infty)$, while the H-derived optical modes contribute to ≈85 (90)% of λ. Specifically, $\lambda(\omega)$ arising from H-derived phonon modes monotonically increases with

Table 2. Estimated components $N_j(E_F)$, I_j^2, and $M\omega_{2,j}^2$ that determine λ_j (j = Th, H) in ThH_9 and ThH_{18}. The estimated values for ω_{log} and T_c arising from Th and H atoms are also given. Here, T_c values are estimated using the McMillan–Allen–Dynes formula.[68] For comparison, the T_c value estimated using the isotropic Eliashberg equations is given in the last column.

		ω_{log} [cm^{-1}]	$N(E_F)$ [eV^{-1}]	I^2 [$eV^2Å^{-2}$]	$M\omega_2^2$ [$eV Å^{-2}$]	λ	T_c [K]	T_c (Figure 5) [K]
ThH_9	Th	135	0.444	7.282	13.876	0.233	0	151
	H	885	0.382	1.461	0.423	1.319	139	–
ThH_{18}	Th	151	0.421	7.904	16.153	0.206	0	269
	H	1034	0.715	1.428	0.545	1.874	240	–

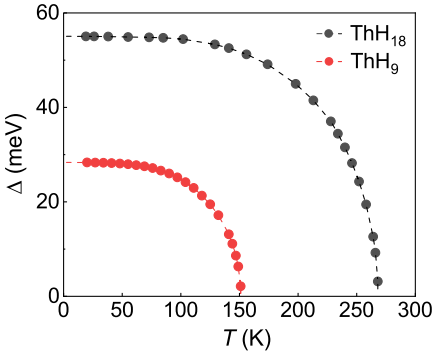

Figure 5. Calculated superconducting gaps Δ of ThH_9 and ThH_{18} as a function of temperature with $\mu^* = 0.1$.

increasing frequency. Therefore, ThH_{18} having higher H content reaches a much larger value of $\lambda = 2.08$,[61,62] compared to that (1.55) of ThH_9 (see Figure 4a,b). By numerically solving the isotropic Eliashberg equations[59] with the typical Coulomb pseudopotential parameter of $\mu^* = 0.1$,[36] we obtain the temperature dependence of superconducting gap Δ (see **Figure 5**). For ThH_9, we find that Δ closes at a T_c of ≈151 K at 130 GPa, in good agreement with the measured value of 146 K at 170–175 GPa.[33] Meanwhile, for ThH_{18}, the estimated T_c is as high as ≈269 K, being comparable with that (296 K) of a previous theoretical calculation.[36] Here, we note that the anisotropy in Δ enhances T_c due to the existence of multiple Fermi surfaces[63] in ThH_9 and ThH_{18}.[64] Furthermore, we calculate the Δ versus T relation with respect to μ^*. Figure S9, Supporting Information, shows that the estimated values of T_c in ThH_9 (ThH_{18}) are 151 (269), 139 (250), and 128 (235) K with $\mu^* = 0.1$, 0.13, and 0.16, respectively, indicating that T_c decreases monotonically with increasing μ^*. Therefore, T_c of ThH_9 estimated with $\mu^* = 0.1$ agrees well with the experimental data.[33]

To understand why there is a large difference in λ between ThH_9 and ThH_{18}, we compare the contributions of the underlying components that determine λ. Since the frequency ranges of the Th-derived acoustic and H-derived optical modes are well separated (Figure 4a,b), λ can be expressed as a sum of its atom-specific components λ_j (j = Th, H) according to the McMillan–Hopfield theory[65–67] that is

$$\lambda = \int \frac{2}{\omega}\alpha^2 F(\omega)d\omega \quad \rightarrow \quad \sum_j \frac{N_j(E_F)I_j^2}{M_j\omega_{2,j}^2} \tag{1}$$

where $N_j(E_F)$ is the Th- or H-derived DOS at E_F, I_j^2 is the atom-specific Fermi-surface average-squared electron–phonon matrix element, M is the atomic mass, and $\omega_{2,j}^2$ is the atom specific average-squared phonon frequency. Therefore, λ_j is composed of the electronic part $N_j(E_F)I_j^2$ in the numerator of Equation (1) and the phonon part $M_j\omega_{2,j}^2$ in the denominator. For ThH_9 and ThH_{18}, each component contributing to λ_j is listed in Table 2. Using the McMillan–Allen–Dynes formula,[68] we can estimate T_c from λ_j and ω_{log} associated with each atom.[65] Although the McMillan–Allen–Dynes formula usually underestimates T_c,[69–73] its estimation may provide a qualitative aspect of how largely certain phonon modes contribute to T_c. As shown in Table 2, the acoustic phonon modes of Th atoms contribute to an increase in λ, but they hardly increase T_c, similar to the cases of other high-T_c hydrides.[65,71] Since λ_{Th} is insensitive to an increase in T_c, we examine how $N_H(E_F)$, I_H^2, and $M_H\omega_{2,H}^2$ for H atom contribute to λ_H that mostly determines T_c. In Table 2, we find that 1) $N_H(E_F)$ is ≈1.87 times larger in ThH_{18} than in ThH_9, 2) $M_H\omega_{2,H}^2$ is ≈29% larger in ThH_{18} than in ThH_9, and 3) I_H^2 in ThH_{18} is similar between the two hydrides. Consequently, we can say that for ThH_{18}, λ_H is dominantly increased by $N_H(E_F)$ despite its lowering via $M_H\omega_{2,H}^2$ [see Equation (1)], resulting in a higher T_c compared to ThH_9.

Finally, we examine the pressure effect on the bonding characteristics of ThH_9 and ThH_{18} by comparing their PDOS values at the same pressure of 400 GPa. As shown in Figure S10a, Supporting Information, the Th 6*p* semicore states in ThH_9 are substantially delocalized to hybridize with the H 1*s* state in a wide energy range between −26 eV and E_F, like those in ThH_{18} (see Figure 2d). It is thus likely that the large delocalization of Th 6*p* semicore electrons in ThH_{18} is associated with the increased interactions between Th and H atoms at a high pressure of 400 GPa. Meanwhile, the band dispersion of ThH_9 at 400 GPa (see Figure S10b, Supporting Information) shows a little change around E_F compared to that at 130 GPa (see Figure 2a). We find that the magnitude of H-derived DOS $N_H(E_F)$ in ThH_9 becomes 0.348 states/eV at 400 GPa, which is comparable with that (0.382 states/eV) at 130 GPa. The former value of $N_H(E_F)$ in ThH_9 is ≈2.05 times smaller than that (0.715 states/eV) in ThH_{18}. Using the Allen–Dynes equation, we predict that ThH_9 has a T_c of ≈126 K at 400 GPa, slightly lower than that (139 K) at 130 GPa. It is thus likely that pressure is insensitive to the T_c difference between ThH_9 and ThH_{18}, while stoichiometry plays an important role in their large difference in T_c.

4. Conclusion

Using first-principles calculations, we have investigated the structural, electronic, phononic, and superconducting properties of ThH_9 and ThH_{18} which showed the very large differences in the stabilization pressure and T_c.[33,36] We found that ThH_9 has a greater ionic bonding character due to more charge transfer from Th to H atoms. Meanwhile, ThH_{18} has a more substantial hybridization of the Th 6*p*-semicore and H 1*s* states, which leads to the stablization of the extremely H-rich H_{36} clathrate cage at higher pressures. Furthermore, we revealed that ThH_{18} has about two times larger H-derived DOS at E_F than ThH_9, which dominantly contributes to enhancing λ and T_c. However, the electron–phonon matrix element was found to make minor contributions to the change of λ between ThH_9 and ThH_{18}. We thus demonstrated that the differences in the bonding character between Th atom and its surrounding H cage reflects the different stabilization pressures of ThH_9 and ThH_{18} and that the H-derived DOS at E_F plays a crucial role in the very large difference in T_c betweeen the two Th hydrides.

Supporting Information

Supporting Information is available from the Wiley Online Library or from the author.

Acknowledgements

S.Y. and C.W. contributed equally to this work. This work was supported by the National Research Foundation of Korea (NRF) grant funded by the Korean Government (grant nos. 2022R1A2C1005456 and RS202300218998), by BrainLink program funded by the Ministry of Science and ICT through the National Research Foundation of Korea (2022H1D3A3A01077468), and by the National Natural Science Foundation of China (grant no. 12074099). The calculations were performed by the KISTI Supercomputing Center through the Strategic Support Program (program no. KSC-2022-CRE-0073) for the supercomputing application research.

Conflict of Interest

The authors declare no conflict of interest.

Data Availability Statement

The data that support the findings of this study are available from the corresponding author upon reasonable request.

Keywords

clathrate thorium hydrides, high-pressures, superconductivities

Received: October 7, 2023
Published online:

[1] T. Bi, N. Zarifi, T. Terpstra, E. Zurek, in *Elsevier Reference Module in Chemistry, Molecular Sciences and Chemical Engineering* (Ed: J. Reedijk), Elsevier, Waltham, MA **2017**.
[2] B. Lilia, R. Hennig, P. Hirschfeld, G. Profeta, A. Sanna, E. Zurek, W. Pickett, M. Amsler, R. Dias, M. Eremets, C. Heil, R. Hemley, H. Liu, Y. Ma, C. Pierleoni, A. Kolmogorov, N. Rybin, D. Novoselov, V. Anisimov, A. Oganov, C. Pickard, T. Bi, R. Arita, I. Errea, C. Pellegrini, R. Requist, E. Gross, E. Margine, S. Xie, Y. Quan, et al., *J. Phys.: Condens. Matter* **2022**, *34*, 183002.
[3] J. Flores-Livas, L. Boeri, A. Sanna, G. Profeta, R. Arita, M. Eremets, *Phys. Rep.* **2020**, *856*, 1.
[4] N. W. Ashcroft, *Phys. Rev. Lett.* **1968**, *21*, 1748.
[5] R. P. Dias, I. F. Silvera, *Science* **2017**, *355*, 715.
[6] P. Loubeyre, F. Occelli, P. Dumas, *Nature* **2020**, *577*, 631.
[7] W. A. Bassett, *High Pressure Res.* **2009**, *29*, 163.
[8] H. K. Mao, X. J. Chen, Y. Ding, B. Li, L. Wang, *Rev. Mod. Phys.* **2018**, *90*, 015007.
[9] N. W. Ashcroft, *Phys. Rev. Lett.* **2004**, *92*, 187002.
[10] Y. Sun, M. Miao, https://ssrn.com/abstract=4108215 (accessed: May 2022).
[11] K. P. Hilleke, E. Zurek, *Angew. Chem., Int. Ed.* **2022**, *61*, e202207589.
[12] A. P. Drozdov, M. I. Eremets, I. A. Troyan, V. Ksenofontov, S. I. Shylin, *Nature* **2015**, *525*, 73.
[13] M. Somayazulu, M. Ahart, A. K. Mishra, Z. M. Geballe, M. Baldini, Y. Meng, V. V. Struzhkin, R. J. Hemley, *Phys. Rev. Lett.* **2019**, *122*, 027001.
[14] A. P. Drozdov, P. P. Kong, V. S. Minkov, S. P. Besedin, M. A. Kuzovnikov, S. Mozaffari, L. Balicas, F. F. Balakirev, D. E. Graf, V. B. Prakapenka, E. Greenberg, D. A. Knyazev, M. Tkacz, M. I. Eremets, *Nature* **2019**, *569*, 528.
[15] I. A. Troyan, D. V. Semenok, A. G. Kvashnin, A. V. Sadakov, O. A. Sobolevskiy, V. M. Pudalov, A. G. Ivanova, V. B. Prakapenka, E. Greenberg, A. G. Gavriliuk, I. S. Lyubutin, V. V. Struzhkin, A. Bergara, I. Errea, R. Bianco, M. Calandra, F. Mauri, L. Monacelli, R. Akashi, A. R. Oganov, *Adv. Mater.* **2021**, *33*, 2006832.
[16] P. Kong, V. S. Minkov, M. A. Kuzovnikov, A. P. Drozdov, S. P. Besedin, S. Mozaffari, L. Balicas, F. F. Balakirev, V. B. Prakapenka, S. Chariton, D. A. Knyazev, E. Greenberg, M. I. Eremets, *Nat. Commun.* **2021**, *12*, 5075.
[17] E. Snider, N. Dasenbrock-Gammon, R. McBride, X. Wang, N. Meyers, K. V. Lawler, E. Zurek, A. Salamat, R. P. Dias, *Phys. Rev. Lett.* **2021**, *126*, 117003.
[18] E. Zurek, R. Hoffmann, N. W. Ashcroft, A. R. Oganov, A. O. Lyakhov, *Proc. Natl. Acad. Sci. USA* **2009**, *106*, 42.
[19] J. Hooper, E. Zurek, *J. Phys. Chem. C* **2012**, *116*, 13322.
[20] H. Wang, J. S. Tse, K. Tanaka, T. Litaka, Y. Ma, *Proc. Natl. Acad. Sci. USA* **2012**, *109*, 6463.
[21] Y. Xie, Q. Li, A. R. Oganov, H. Wang, *Acta Crystallogr., Sect. C: Struct. Chem.* **2014**, *70*, 104.
[22] D. Duan, Y. Liu, F. Tian, D. Li, X. Huang, Z. Zhao, H. Yu, B. Liu, W. Tian, T. Cui, *Sci. Rep.* **2014**, *4*, 6968.
[23] Y. Li, J. Hao, H. Liu, Y. Li, Y. Ma, *J. Chem. Phys.* **2014**, *140*, 174712.
[24] X. Feng, J. Zhang, G. Gao, H. Liu, H. Wang, *RSC Adv.* **2015**, *5*, 59292.
[25] F. Peng, Y. Sun, C. J. Pickard, R. J. Needs, Q. Wu, Y. Ma, *Phys. Rev. Lett.* **2017**, *119*, 107001.
[26] H. Liu, I. I. Naumov, R. Hoffmann, N. W. Ashcroft, R. J. Hemley, *Proc. Natl. Acad. Sci. USA* **2017**, *114*, 6990.
[27] Y. Sun, J. Lv, Y. Xie, H. Liu, Y. Ma, *Phys. Rev. Lett.* **2019**, *123*, 097001.
[28] H. Xie, Y. Yao, X. Feng, D. Duan, H. Song, Z. Zhang, S. Jiang, S. A. T. Redfern, V. Z. Kresin, C. J. Pickard, T. Cui, *Phys. Rev. Lett.* **2020**, *125*, 217001.
[29] H. Cui, M. Li, F. Zheng, P. Zhang, *Phys. Status Solidi B* **2023**, *260*, 2200452.

[30] X. Li, X. Huang, D. Duan, C. J. Pickard, D. Zhou, H. Xie, Q. Zhuang, Y. Huang, Q. Zhou, B. Liu, T. Cui, *Nat. Commun.* **2019**, *10*, 3461.
[31] N. P. Salke, M. M. Davari Esfahani, Y. Zhang, I. A. Kruglov, J. Zhou, Y. Wang, E. Greenberg, V. B. Prakapenka, J. Liu, A. R. Oganov, J.-F. Lin, *Nat. Commun.* **2019**, *10*, 4453.
[32] W. Chen, D. V. Semenok, X. Huang, H. Shu, X. Li, D. Duan, T. Cui, A. R. Oganov, *Phys. Rev. Lett.* **2021**, *127*, 117001.
[33] D. V. Semenok, A. G. Kvashnin, A. G. Ivanova, V. Svitlyk, V. Y. Fominski, A. V. Sadakov, O. A. Sobolwvskiy, V. M. Pudalov, I. A. Troyan, A. R. Oganov, *Mater. Today* **2020**, *33*, 36.
[34] L. Ma, K. Wang, Y. Xie, X. Yang, Y. Wang, M. Zhou, H. Liu, X. Yu, Y. Zhao, H. Wang, G. Liu, Y. Ma, *Phys. Rev. Lett.* **2022**, *128*, 167001.
[35] Z. Li, X. He, C. Zhang, X. Wang, S. Zhang, Y. Jia, S. Feng, K. Lu, J. Zhao, J. Zhang, B. Min, Y. Long, R. Yu, L. Wang, M. Ye, Z. Zhang, V. Prakapenka, S. Chariton, P. A. Ginsberg, J. Bass, S. Yuan, H. Liu, C. Jin, *Nat. Commun.* **2022**, *13*, 2863.
[36] X. Zhong, Y. Sun, T. Iitaka, M. Xu, H. Liu, R. J. Hemley, C. Chen, Y. Ma, *J. Am. Chem. Soc.* **2022**, *144*, 13394.
[37] J. Bardeen, L. N. Cooper, J. R. Schrieffer, *Phys. Rev.* **1957**, *106*, 162.
[38] G. Kresse, J. Hafner, *Phys. Rev. B* **1993**, *48*, 13115.
[39] G. Kresse, J. Furthmüller, *Comput. Mater. Sci.* **1996**, *6*, 15.
[40] P. E. Blöchl, *Phys. Rev. B* **1994**, *50*, 17953.
[41] J. P. Perdew, K. Burke, M. Ernzerhof, *Phys. Rev. Lett.* **1996**, *77*, 3865.
[42] P. Giannozzi, S. Baroni, N. Bonini, M. Calandra, R. Car, C. Cavazzoni, D. Ceresoli, G. L. Chiarotti, M. Cococcioni, I. Dabo, A. Dal Corso, *J. Phys.: Condens. Matter* **2009**, *21*, 395502.
[43] D. Vanderbilt, *Phys. Rev. B* **1990**, *41*, 7892.
[44] We have performed structural optimization using two different pseudopotentials. It is found that the lattice parameters of ThH_9 (ThH_{18}) obtained using PAW pseudopotentials are $a = 3.73$ Å, $b = 3.73$ Å, and $c = 5.57$ Å ($a = 3.36$ Å, $b = 5.83$ Å, and $c = 7.18$ Å), very close to $a = 3.72$ Å, $b = 3.72$ Å, and $c = 5.56$ Å ($a = 3.35$ Å, $b = 5.82$ Å, and $c = 7.18$ Å) obtained using ultrasoft pseudopotentials. Therefore, as shown in Figure S1, Supporting Information, the band structures of ThH_9 and ThH_{18} obtained using the two pseudopotentials are nearly identical to each other.
[45] F. Giustino, M. L. Cohen, S. G. Louie, *Phys. Rev. B* **2007**, *76*, 165108.
[46] S. Poncé, E. R. Margine, C. Verdi, F. Giustino, *Comput. Phys. Commun.* **2016**, *209*, 116.
[47] The T_c-convergence test for ThH_{18} with respect to the number of q and k points shows that the T_c is well converged with $6 \times 6 \times 6$ q and $24 \times 24 \times 24$ k points (see Figure S2, Supporting Information). These numbers of q and k points are more than those ($4 \times 4 \times 4$ q and $8 \times 8 \times 8$ k points: see the mark "×" in Figure S2, Supporting Information) used in a previous DFT calculation by Zhong et al. [36].
[48] It is noted that the La 5p semicore electrons in high-pressure LaH_{10} are significantly delocalized to hybridize with H 1s state.[49,52] To demonstrate how Th 6p electrons are delocalized with increasing pressure, we compare the PDOS of ThH_9 at 130, 200, and 400 GPa. As shown in Figure S3, Supporting Information, the energy range of delocalized Th 6p states in ThH_9 increases with increasing pressure.
[49] D. A. Papaconstantopoulos, M. J. Mehl, P.-H. Chang, *Phys. Rev. B* **2020**, *101*, 060506.
[50] It is noted that the comparison of covalent bonding strengths between ThH_9 and ThH_{18} could be related to their bond lengths. We find that ThH_9 has Th—H (H—H) bond lengths of 2.08–2.23 (1.10–1.45) Å (see Figure 1a), which are longer than 1.88–2.04 (1.00–1.19) Å (see Figure 1b) in ThH_{18}. Meanwhile, the corresponding Th—H (H—H) bond lengths in ThH_9 at 400 GPa become 1.90–2.01 (0.97–1.23) Å, close to those in ThH_{18}.
[51] To confirm that the PDOS plots in Figure 2c,d are sufficiently converged with respect to the k points employed for the integration over the Brillouin zone, we calculated the PDOS of ThH_9 and ThH_{18} by further increasing the number of the k-point meshes. As shown in Figure S4, Supporting Information, the PDOS of ThH_9 (ThH_{18}) obtained with the $24 \times 24 \times 18$ ($18 \times 18 \times 18$) k points is nearly the same as that with the $48 \times 48 \times 36$ ($32 \times 32 \times 32$) k points. We also compare the PDOS of ThH_9 and ThH_{18} with the unit of states/(eV, atom, spin): see Figure S5, Supporting Information. Here, we find that the $N_H(E_F)$ value in ThH_{18} is ≈1.99 times larger than that in ThH_9. This ratio is close to that (≈1.87) of $N_H(E_F)$ between ThH_9 and ThH_{18}, obtained with the unit of state/eV per unit cell (see Table 2). It is noted that, for ThH_{18}, we obtain the total DOS $N(E_F)$ at the Fermi level as ≈0.030 states/(eV, atom, spin), in good agreement with that (≈0.027) of a previous DFT calculation [36].
[52] S. Yi, C. Wang, H. Jeon, J.-H. Cho, *Phys. Rev. Mater.* **2021**, *5*, 024801.
[53] S. Yao, C. Wang, S. Liu, H. Jeon, J.-H. Cho, *Inorg. Chem.* **2021**, *60*, 12934.
[54] R. F. W. Bader, *Acc. Chem. Res.* **1985**, *18*, 9.
[55] W. Tang, E. Sanville, G. Henkelman, *J. Phys.: Condens. Matter* **2009**, *21*, 084204.
[56] It is noted that the cationic/anionic charges of the Th/H Bader basins are estimated from the $200 \times 200 \times 320$ ($240 \times 200 \times 180$) meshes in the unit cell of ThH_9 (ThH_{18}). Here, the k-space integration for the charge density of ThH_9 (ThH_{18}) was done with the $18 \times 18 \times 12$ ($8 \times 8 \times 8$) k points.
[57] Figure S6, Supporting Information, shows the animation of the phonon modes with strong EPC strength: i.e., the E_{2g}-symmetry mode at a frequency of 733.8 cm^{-1} for ThH_9 and the Ag-symmetry mode at a frequency of 699 cm^{-1} for ThH_{18}.
[58] A. B. Migdal, *Sov. Phys. JETP* **1958**, *34*, 6.
[59] G. M. Eliashberg, *Sov. Phys. JETP* **1960**, *11*, 3.
[60] P. B. Allen, B. Mitrović, *Solid State Phys.* **1982**, *37*, 1.
[61] For the integration of the Eliashberg function, we use a smearing width Sw of 0.1 eV in the double delta function. Using a smaller smearing width $S_w = 0.05$ eV, we obtain the EPC constant $\lambda = 2.22$, close to that (2.08) with $S_w = 0.1$ eV. Therefore, we can say that λ little changes with respect to smearing width.
[62] It is noted that the experimentally synthesized LaH_{10} [65], YH_6 [15] and CaH_6 [65] have λ values larger than 2, leading to high T_c reaching 203, 260, and 215 K, respectively.
[63] Figure S7a,b, Supporting Information, show the calculated Fermi surfaces of ThH_9 and ThH_{18}, respectively. Each Fermi surface is composed of four sheets (designated as FS1, FS2, FS3, and FS4). For ThH_9, FS1 forms small patches, FS2 forms complex shapes, FS3 forms the cylindrical–like sheet surrounding the γ–A path, and FS4 forms the spherical-like sheet around the γ point. Meanwhile, for ThH_{18}, FS1 and FS2 show similar patterns as those of ThH_9, whereas FS3 forms largely deformed cylindrical-like sheet surrounding the γ–Z path, and FS4 forms the small pockets around the Z point.
[64] By numerically solving the anisotropic Migdal-Eliashberg equations with a Coulomb pseudopotential parameter of $\mu^* = 0.1$, we calculate the temperature dependence of the anisotropic superconducting gap Δ in ThH_9 and ThH_{18}. Figure S8, Supporting Information, displays the energy distribution of Δ as a function of temperature. We find that the widely distributed Δ closes at $T_c = 162$ (300) K in ThH_9 (ThH_{18}), which is higher than the isotropic superconducting gap value of 151 (269) K. It is noted that the anisotropy in Δ is larger in ThH_{18} than in ThH_9. The detailed analysis for the band-resolved and *k*-resolved anisotropy of Δ needs to be explored in future work.
[65] Y. Quan, S. S. Ghosh, W. E. Pickett, *Phys. Rev. B* **2019**, *100*, 184505.
[66] W. L. McMillan, *Phys. Rev.* **1968**, *167*, 331.
[67] J. J. Hopfield, *Phys. Rev.* **1969**, *186*, 443.

[68] P. B. Allen, R. C. Dynes, *Phys. Rev. B* **1975**, *12*, 905.
[69] S. Xie, Y. Quan, A. Hire, B. Deng, J. DeStefano, I. Salinas, U. Shah, L. Fanfarillo, J. Lim, J. Kim, G. Stewart, J. Hamlin, P. Hirschfeld, R. Hennig, *npj Comput. Mater.* **2022**, *8*, 14.
[70] C. Wang, S. Yi, J.-H. Cho, *Phys. Rev. B* **2019**, *100*, 060502.
[71] C. Wang, S. Yi, J.-H. Cho, *Phys. Rev. B* **2020**, *101*, 104506.
[72] A. P. Durajski, R. Szczesniak, Y. Li, C. Wang, J.-H. Cho, *Phys. Rev. B* **2020**, *101*, 214501.
[73] C. Wang, S. Liu, H. Jeon, S. Yi, Y. Bang, J.-H. Cho, *Phys. Rev. B* **2021**, *104*, L020504.